

Supplementary Material to “Imaging Interiors: An Implicit Solution to Electromagnetic Inverse Scattering Problems”

Ziyuan Luo¹, Boxin Shi^{2,3}, Haoliang Li⁴, and Renjie Wan¹

¹ Department of Computer Science, Hong Kong Baptist University

² State Key Laboratory for Multimedia Information Processing,
School of Computer Science, Peking University

³ National Engineering Research Center of Visual Technology,
School of Computer Science, Peking University

⁴ Department of Electrical Engineering, City University of Hong Kong
ziyuanluo@life.hkbu.edu.hk, shiboxin@pku.edu.cn, haoliang.li@cityu.edu.hk,
renjiewan@hkbu.edu.hk

S1 Overview

This supplementary document provides more discussions, reproduction details, and additional results that accompany the main paper:

- Sec. S2 discusses the detailed physical model of the Electromagnetic Inverse Scattering Problems (EISP).
- Sec. S3 provides details of the system settings for each dataset.
- Sec. S4 presents reproduction details and pseudocode of our method.
- Sec. S5 provides additional results, including ablation studies on different backbones and variation loss, and additional qualitative and quantitative results.

S2 Detailed physical model of EISP

To clarify the physical model of the EISP, we copy some key equations in the main paper here. The data equation describes the wave-scatterer interaction, which can be formulated as

$$\mathbf{E}^t = \mathbf{E}^i + \mathbf{G}_D \cdot \mathbf{J}, \quad (\text{S1})$$

where \mathbf{E}^t , \mathbf{E}^i , and \mathbf{J} are the discrete total electric fields, incident electric fields, and induced current, respectively. \mathbf{G}_D is discrete free space Green’s function in Region of Interest (ROI) D . The relationship between the induced current \mathbf{J} and total electric fields \mathbf{E}^t can be described as

$$\mathbf{J} = \text{Diag}(\boldsymbol{\xi}) \cdot \mathbf{E}^t, \quad (\text{S2})$$

where $\text{Diag}(\boldsymbol{\xi})$ is the diagonal matrix of the contrast function. The contrast $\boldsymbol{\xi}$ is defined as

$$\boldsymbol{\xi} = \boldsymbol{\varepsilon}_{\mathbf{r}} - 1, \quad (\text{S3})$$

where $\boldsymbol{\varepsilon}_{\mathbf{r}}$ is the relative permittivity. The data equation describes the scattered field as a reradiation of the induced current, which can be expressed as

$$\mathbf{E}^{\text{s}} = \mathbf{G}_S \cdot \mathbf{J}, \quad (\text{S4})$$

where \mathbf{E}^{s} is the discrete scattered field, and \mathbf{G}_S is the discrete Green's function to map the induced current \mathbf{J} to scattered field \mathbf{E}^{s} .

S2.1 Forward estimation

The aim of forward estimation is to deduce the scattered fields \mathbf{E}^{s} from given incident fields \mathbf{E}^{i} . The forward estimation is linear because \mathbf{E}^{s} and \mathbf{E}^{i} have a linear relationship [4]. Specifically, by replacing \mathbf{J} in Eq. (S1) with Eq. (S2), we can obtain

$$\mathbf{E}^{\text{t}} = \mathbf{E}^{\text{i}} + \mathbf{G}_D \cdot \text{Diag}(\boldsymbol{\xi}) \cdot \mathbf{E}^{\text{t}}. \quad (\text{S5})$$

Reformulating Eq. (S5) yields the expression for total fields \mathbf{E}^{t} :

$$\mathbf{E}^{\text{t}} = (\mathbf{I} - \mathbf{G}_D \text{Diag}(\boldsymbol{\xi}))^{-1} \cdot \mathbf{E}^{\text{i}}. \quad (\text{S6})$$

By combining Eq. (S2), we can obtain the expression of induced current \mathbf{J} as

$$\mathbf{J} = \text{Diag}(\boldsymbol{\xi}) \cdot (\mathbf{I} - \mathbf{G}_D \text{Diag}(\boldsymbol{\xi}))^{-1} \cdot \mathbf{E}^{\text{i}}. \quad (\text{S7})$$

Then, the expression for the scattered fields \mathbf{E}^{s} can be obtained from Eq. (S4) and Eq. (S7) as

$$\mathbf{E}^{\text{s}} = \mathbf{G}_S \cdot \text{Diag}(\boldsymbol{\xi}) \cdot (\mathbf{I} - \mathbf{G}_D \text{Diag}(\boldsymbol{\xi}))^{-1} \cdot \mathbf{E}^{\text{i}}. \quad (\text{S8})$$

Since Green's functions \mathbf{G}_D and \mathbf{G}_S are fixed in our problem, and the contrast $\boldsymbol{\xi}$, or relative permittivity $\boldsymbol{\varepsilon}_{\mathbf{r}}$ is the physical property independent of the incident fields, Eq. (S8) is a linear equation in variables \mathbf{E}^{s} and \mathbf{E}^{i} . Therefore, we can easily obtain the scattered fields \mathbf{E}^{s} through Eq. (S8) if the relative permittivity $\boldsymbol{\varepsilon}_{\mathbf{r}}$ is known. We propose to make use of the convenience and benefits of the forward estimation to circumvent the difficulties of EISP.

S2.2 Difficulties of EISP

In this section, we discuss three main challenges of EISP and explain why our approach can address these challenges.

Inverse. In an inverse problem, the incident fields \mathbf{E}^i are given, and the scattered fields \mathbf{E}^s are measured by receivers, and then the task is to reconstruct relative permittivity ε_r from the measured scattered fields. From Eq. (S3), this task is equivalent to predicting the contrast ξ . An intuitive approach is to infer the induced current \mathbf{J} from the scattered field \mathbf{E}^s by inverse deduction from Eq. (S4). However, the discrete Green’s function is a complex matrix of dimension $N_r \times M^2$, where N_r is the total number of receivers and $M \times M$ is the size of the discretized subunits of ROI. In practice, we have $N_r \ll M^2$. Since such a less-than relation does not provide enough information to determine \mathbf{J} from Eq. (S4), it is difficult to obtain relative permittivity ε_r in this inverse way.

Nonlinearity. The nonlinearity poses significant challenges to the solution of the EISP. We explain nonlinearity from two perspectives. First, in Eq. (S8), the nonlinearity is due to the fact that the scattered fields \mathbf{E}^s are not doubled when the scatterer’s permittivity is doubled. This phenomenon is caused by the condition that total fields E_t is a quantity related to the relative permittivity ε_r according to Eq. (S6). Then, The nonlinearity is due to the multiple scattering effects that physically exist. In Eq. (S1), the global-effect term $\mathbf{G}_D \cdot \mathbf{J}$ is caused by multiple scattering effects [4], a factor leading to the nonlinearity. Traditional methods, such as Born approximation [8, 16], involve a linearization of the original problem by neglecting the effect of multiple scattering. However, these methods can introduce significant errors and compromise the accuracy of the computation when the multiple scattering amplitude is large and unignorable.

Discretization. Although the relative permittivity ε_r exhibits continuous properties, numerical computations based on the aforementioned discrete equations can only obtain the discrete form of the relative permittivity with low resolution. Such a low resolution always makes it difficult to recognize the scatterer’s details.

Why can our approach address these challenges? We propose an implicit forward solution for EISP. First, we apply Implicit Neural Representations (INR) to represent relative permittivity ε_r and induced current J separately. Then we optimize these two representations through forward estimation by constructing two loss functions, namely data loss $\mathcal{L}_{\text{data}}$ and state loss $\mathcal{L}_{\text{state}}$. In this way, we do not need to worry about the difficulties caused by inverse estimation and nonlinearity. Besides, due to the inherent property of INR to approximate continuous functions, our method can provide results with flexible resolutions.

S3 Details of system settings

We conduct our experiments on Synthetic, real-world, and 3D datasets. There are some differences in system settings for each dataset, and we provide separate explanations for each.

S3.1 Settings for synthetic datasets

Two synthetic datasets, the Circular-cylinder dataset and the MNIST dataset [18, 20], are used for our experiments. The basic settings are the same for these two datasets. We set operating frequency $f = 400$ MHz, and the ROI is a square with the size of $2 \times 2\text{m}^2$. The placement scheme for transmitters and receivers is illustrated in Fig. S1. There are 16 transmitters and 32 receivers equally placed on a circle of radius 3 m centered at the center of ROI.

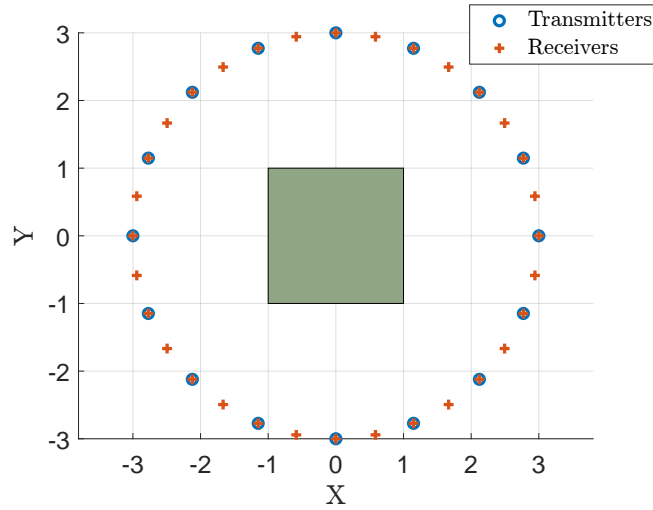


Fig. S1: Positions of the transmitters and receivers on the measurement circle for synthetic datasets. The green area indicates the ROI.

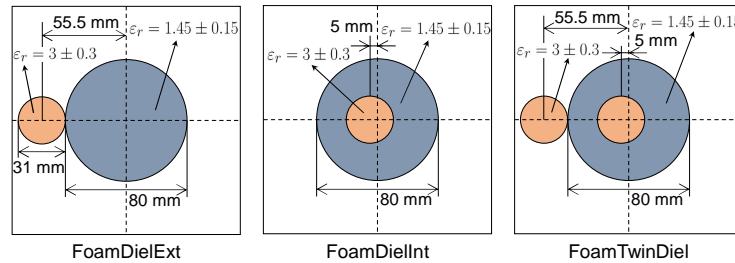


Fig. S2: The ground truth of FoamDielExt, FoamDielInt, and FoamTwinDiel scenarios in Institut Fresnel's database [7].

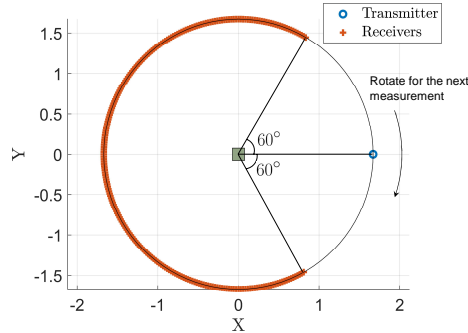


Fig. S3: Positions of the transmitters and receivers on the measurement circle for Institut Fresnel’s database [7]. For FoamDielExt/FoamDielInt and FoamTwinDiel, the measurement system rotates by 45° and 20° , respectively, for the next measurement. The green area indicates the ROI.

S3.2 Settings for real-world dataset

Institut Fresnel’s database [7] is a famous real-world electromagnetic scattering dataset in the field of EISP. We use FoamDielExt, FoamDielInt, and FoamTwinDiel scenarios in Institut Fresnel’s database for testing. As presented in Fig. S2, all the cases consist of two kinds of cylinders. The large cylinder (SAITEC SBF 300) has a diameter of 80 mm with the relative permittivity $\varepsilon_r = 1.45 \pm 0.15$. The small cylinder (berylon) has a diameter of 31 mm with the relative permittivity $\varepsilon_r = 3 \pm 0.3$. The “ \pm ” indicates the range of uncertainty associated with the experimental value. The operating frequencies are taken from 2 to 10 GHz with a step of 1 GHz. The ROI is a square with the size of $0.15 \times 0.15\text{m}^2$. All the transmitters and receivers are equally placed on a circle of radius 1.67 m centered at the center of ROI. For all scenarios, 241 receivers are used for each measurement, with a central angle step of 1° , without any position closer than 60° from the transmitter [7]. The placement schemes for FoamDielExt, FoamDielInt, and FoamTwinDiel are shown in Fig. S3. After each measurement, the measurement system rotates by a certain angle for the next measurement. For FoamDielExt and FoamDielInt, this angle is 45° , while for FoamTwinDiel, it is 20° . This means there are 8 transmitters for FoamDielExt and FoamDielInt, while there are 18 transmitters for FoamTwinDiel.

S3.3 Settings for 3D dataset

We also test our method on the 3D MNIST dataset [9]. We set the permittivities of the objects to be 2. We set operating frequency $f = 400\text{ MHz}$, and the ROI is a cube with the size of $2 \times 2 \times 2\text{m}^3$. As shown in Fig. S4, there are 40 transmitters and 160 receivers. The transmitters and receivers are all located at the sphere of radius 3 m around the target centered at the center of ROI. For the positions of transmitters, the azimuthal angle ranged from 0° to 315° with a 45° step, and

the polar angle ranged from 30° to 150° with a 30° step. For the positions of receivers, the azimuthal angle ranged from 0° to 348.75° with an 11.25° step, and the polar angle ranged from 30° to 150° with a 30° step.

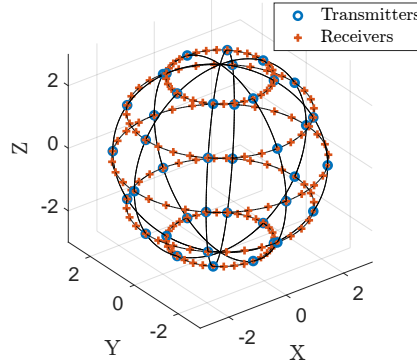


Fig. S4: Positions of the transmitters and receivers on the measurement sphere for 3D dataset.

S4 Reproduction details and Pseudocode

S4.1 Reproduction details

In this section, we present reproduction details and pseudocode of our method. Our code will be released upon the acceptance of this paper.

Additional network details. Two eight-layer MLPs with 256 channels and ReLU activations are used to individually predict the relative permittivity ε_r and induced current J . The difference between these two networks lies in the last layer. The output dimension of the last layer is 1 for relative permittivity and 2 for induced current, representing the real and imaginary parts, respectively.

Computational details. In Section 4.2, we have developed formulas to predict the relative permittivity and induced current for each transmitter. Specifically, for p -th transmitter, we can obtain the predicted scattered fields as

$$\hat{\mathbf{E}}_p^s = \mathbf{G}_S \cdot \mathbf{J}_p, \quad p = 1, 2, \dots, N_t, \quad (\text{S9})$$

where \mathbf{G}_S is a $N_r \times M^2$ complex matrix, denoting the discrete Green's function, and \mathbf{J}_p and $\hat{\mathbf{E}}_p^s$ are complex vectors of dimensions M^2 and N_r , denoting the discrete induced current and predicted scattered fields inspired by p -th transmitter, respectively. N_t and N_r are the total numbers of transmitters and receivers, respectively, and $M \times M$ is the size of the discretized subunits of ROI. \mathbf{J}_p is the

discrete induced current directly sampled from H_ϕ . To calculate the mismatch of the state equation, we can obtain the predicted induced current $\hat{\mathbf{J}}_p$ as

$$\hat{\mathbf{J}}_p = \text{Diag}(\boldsymbol{\xi}) \cdot \mathbf{E}_p^i + \text{Diag}(\boldsymbol{\xi}) \cdot \mathbf{G}_D \cdot \mathbf{J}_p, \quad p = 1, 2, \dots, N_t, \quad (\text{S10})$$

where $\boldsymbol{\xi}$ is a vector of dimension M^2 , reshaped from spatially queried network F_θ , representing the contrast value. $\hat{\mathbf{J}}_p$ is a complex vector of dimension M^2 , indicating the induced current computed via the mathematical correlation. $\text{Diag}(\boldsymbol{\xi})$ is the diagonal matrix of the contrast function with dimension $M^2 \times M^2$. \mathbf{G}_D is also a discrete Green's function with dimension $M^2 \times M^2$.

Although we provide the computation formulas for each transmitter when calculating Eq. (S9) and Eq. (S10) for all N_t transmitters, we use a more efficient approach. To be precise, equations in Eq. (S9) and Eq. (S10) can be rewritten as

$$\hat{\mathbf{E}}_{\text{all}}^s = \mathbf{G}_S \cdot \mathbf{J}_{\text{all}}, \quad (\text{S11})$$

and

$$\hat{\mathbf{J}}_{\text{all}} = \text{Diag}(\boldsymbol{\xi}) \cdot \mathbf{E}_{\text{all}}^i + \text{Diag}(\boldsymbol{\xi}) \cdot \mathbf{G}_D \cdot \mathbf{J}_{\text{all}}, \quad (\text{S12})$$

where

$$\hat{\mathbf{E}}_{\text{all}}^s = [\hat{\mathbf{E}}_1^s, \hat{\mathbf{E}}_2^s, \dots, \hat{\mathbf{E}}_{N_t}^s], \quad (\text{S13})$$

$$\mathbf{J}_{\text{all}} = [\mathbf{J}_1, \mathbf{J}_2, \dots, \mathbf{J}_{N_t}], \quad (\text{S14})$$

$$\hat{\mathbf{J}}_{\text{all}} = [\hat{\mathbf{J}}_1, \hat{\mathbf{J}}_2, \dots, \hat{\mathbf{J}}_{N_t}], \quad (\text{S15})$$

$$\mathbf{E}_{\text{all}}^i = [\mathbf{E}_1^i, \mathbf{E}_2^i, \dots, \mathbf{E}_{N_t}^i]. \quad (\text{S16})$$

In Eq. (S11) and Eq. (S12), $\hat{\mathbf{E}}_{\text{all}}^s$ is a matrix of dimension $N_r \times N_t$, containing the scattered fields referring to all transmitters. \mathbf{J}_{all} , $\hat{\mathbf{J}}_{\text{all}}$, and $\mathbf{E}_{\text{all}}^i$ are all $M^2 \times N_t$ matrices. Therefore, during implementation, the loss functions can be equivalently rewritten as

$$\mathcal{L}_{\text{data}} = \frac{\|\hat{\mathbf{E}}_{\text{all}}^s - \mathbf{E}_{\text{all}}^s\|_2^2}{\|\mathbf{E}_{\text{all}}^s\|_2^2}, \quad (\text{S17})$$

and

$$\mathcal{L}_{\text{state}} = \frac{\|\hat{\mathbf{J}}_{\text{all}} - \mathbf{J}_{\text{all}}\|_2^2}{\|\text{Diag}(\boldsymbol{\xi}) \cdot \mathbf{E}_{\text{all}}^i\|_2^2 + \Delta}, \quad (\text{S18})$$

where $\mathbf{E}_{\text{all}}^s$ is the ground truth measured by receivers in a matrix form, Δ denotes a small number to improve stability by preventing the denominator from being zero, and $\|\cdot\|_2$ denotes the matrix 2-norm.

Calculation of Green’s functions. The two-dimensional scalar Green’s function [4] can be expressed as

$$g(\mathbf{x}, \mathbf{x}') = \frac{i}{4} H_0^{(1)}(k_0 |\mathbf{x} - \mathbf{x}'|), \quad (\text{S19})$$

where $H_0^{(1)}(\cdot)$ is the zeroth order Hankel function of the first kind, $k_0 = 2\pi/\lambda_0$ is the wavenumber in free space, and λ_0 is the wavelength in free space. \mathbf{x} and \mathbf{x}' are the coordinates of two corresponding positions.

We use the method of moment (MOM) [13] with the pulse basis function and the delta testing function to discretize the domain D into $M \times M$ subunit, and the centers of subunits are located at \mathbf{x}_n with $n = 1, 2, \dots, M^2$. Then, we can discretize this continuous Green’s function into matrix \mathbf{G}_D and \mathbf{G}_S respectively. The element in the n -th row and n' -th column of the $M \times M$ matrix \mathbf{G}_D can be obtained as

$$\mathbf{G}_D(n, n') = k_0^2 A_{n'} g(\mathbf{x}_n, \mathbf{x}_{n'}), \quad n = 1, 2, \dots, M^2, n' = 1, 2, \dots, M^2, \quad (\text{S20})$$

where $A_{n'}$ is the area of the n' -th subunits. Similarly, the element in the q -th row and n' -th column of the $N_r \times M$ matrix \mathbf{G}_S can be obtained as

$$\mathbf{G}_S(q, n') = k_0^2 A_{n'} g(\mathbf{x}_q, \mathbf{x}_{n'}), \quad q = 1, 2, \dots, N_r, n' = 1, 2, \dots, M^2. \quad (\text{S21})$$

The discretized forms of Green’s function can then be used in the calculations in Eq. (S9) to Eq. (S12).

Preprocessing for real-world dataset. To handle real-world and synthetic data in a unified manner, we calibrate the real-world data before using it. Following previous works [10, 11, 18], the calibration of real-world scattering field data can be conducted by multiplying those data with a complex coefficient. The complex coefficient is derived by dividing the measured incident field by the simulated incident field at the receiver located opposite the source [7].

Implementation details of baselines. For Physics-Net [11], we follow the formulation in [11] to get the regularization parameter β . We use the backbone architecture depicted in the same paper. For network optimization, we use the SDG optimizer with momentum 0.99, a learning rate 5×10^{-6} that decays following the step scheduler with step size 20 and decay factor 0.5. All the hyperparameters are recommended in the paper.

For PGAN [17], the structure of the generator and discriminator follows the architecture in [17], respectively. We also use the hyperparameters suggested in the paper. The number of hidden layers used in perceptual adversarial loss is $M_d = 1$, weight parameters $\beta = 0.01$ and $\gamma = 4.0$ for the loss function of the generator, and $m = 0.2$ for the loss function of the discriminator. For network optimization, we employ the Adam optimizer with default values $\beta_1 = 0.9$, $\beta_2 = 0.999$, $\epsilon = 10^{-8}$, and a learning rate 2×10^{-4} that decays following the linear scheduler after the first 20 epochs during optimization. All the hyperparameters are the ones suggested by the paper.

We directly use the codes of BPS and CS-Net to ensure the fairness of the evaluation.

S4.2 Pseudocode

We provide a pseudocode to offer a detailed and step-by-step understanding of our proposed approach, as shown in Algorithm S1.

Algorithm S1: Our INR-based method for EISP

- Data:** Incident field \mathbf{E}^t , scattered field \mathbf{E}^s , ROI D , transmitters' positions \mathbf{x}^t , and receivers' positions \mathbf{x}^r
- Result:** Optimized INR F_θ for the object's relative permittivity
- 1 Initial INR F_θ for relative permittivity, and INR H_ϕ for induced current;
 - 2 Generate \mathbf{G}_D and \mathbf{G}_S from \mathbf{x}^t , \mathbf{x}^r and D according to definition of discretized forms of Green's function from Eq. (S20) and Eq. (S21), respectively;
 - 3 **For** step = 1 **to** max_iter:
 - 4 Infer contrast $\boldsymbol{\xi}$ from F_θ using D , and infer induced current \mathbf{J} from H_ϕ using D and \mathbf{x}^t with random spatial sampling;
 - 5 Calculate $\hat{\mathbf{E}}^s$ and $\hat{\mathbf{J}}$ from Eq. (S11) and Eq. (S10), respectively;
 - 6 Calculate $\mathcal{L}_{\text{data}}$, $\mathcal{L}_{\text{state}}$ and \mathcal{L}_{TV} from Eq. (S17), Eq. (S18) and total variation function, respectively;
 - 7 Obtain the loss $\mathcal{L} = \lambda_{\text{data}}\mathcal{L}_{\text{data}} + \lambda_{\text{state}}\mathcal{L}_{\text{state}} + \lambda_{\text{TV}}\mathcal{L}_{\text{TV}}$;
 - 8 Update θ and ϕ by minimizing \mathcal{L} using the Adam optimizer.
-

S5 Additional results

Ablation study on different backbones. We study two different backbones for INR, namely basic MLP with ReLU activations and SIREN [15]. These two structures are both based on fully connected networks to represent continuous mappings, so choosing either network does not affect our proof of the applicability of INR. The results for different backbones are shown in Fig. S5. From the results, both basic MLP and SIREN can accurately reconstruct the internal structures of objects. The reconstruction quality using basic MLP is slightly better than that of SIREN.

Some previous studies point out that SIREN [15] has certain drawbacks in terms of its implementation [5]. First, it cannot utilize the speed-up techniques of INRs, such as the one described in Instant-NGP [12]. Second, their custom activations are still not compatible with accelerator hardware in certain devices [5]. Therefore, we choose the basic MLP as the backbone of INR in our main paper.

Ablation study on variation loss. We further test the impact of total variation loss \mathcal{L}_{TV} for relative permittivity $\boldsymbol{\xi}$ on the results. We show the results with and without \mathcal{L}_{TV} in Fig. S5. The results indicate that \mathcal{L}_{TV} improves our model's performance.

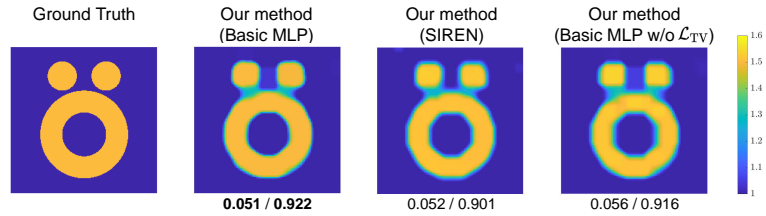


Fig. S5: Ablation study results including comparison with different backbones and comparison with and without variation loss \mathcal{L}_{TV} . We show the results of a standard test case [1] in EISP. The pixel values in the images indicate the values of the relative permittivity. RRMSE/SSIM values are shown below the figure.

Additional qualitative and quantitative results. We present more qualitative and quantitative results on the Circular-cylinder dataset [18] and MNIST dataset [6] under different noise levels, as shown in Fig. S6 to Fig. S9. Our method reaches the highest visual quality compared with the other baseline methods.

References

1. Belkebir, K., Tijhuis, A.: Using multiple frequency information in the iterative solution of a two-dimensional nonlinear inverse problem. In: Proceedings Progress in Electromagnetics Research Symposium (1996)
2. Belkebir, K., Chaumet, P.C., Sentenac, A.: Superresolution in total internal reflection tomography. *Journal of the Optical Society of America A* (2005)
3. Chen, X.: Subspace-based optimization method for solving inverse-scattering problems. *IEEE Transactions on Geoscience and Remote Sensing* (2009)
4. Chen, X.: Computational methods for electromagnetic inverse scattering. John Wiley & Sons (2018)
5. Conde, M.V., Vazquez-Corral, J., Brown, M.S., Timofte, R.: Nilut: Conditional neural implicit 3D lookup tables for image enhancement. In: Proceedings of the AAAI Conference on Artificial Intelligence (2024)
6. Deng, L.: The MNIST database of handwritten digit images for machine learning research. *IEEE Signal Processing Magazine* (2012)
7. Geffrin, J.M., Sabouroux, P., Eyraud, C.: Free space experimental scattering database continuation: experimental set-up and measurement precision. *inverse Problems* (2005)
8. Habashy, T.M., Groom, R.W., Spies, B.R.: Beyond the born and rytov approximations: A nonlinear approach to electromagnetic scattering. *Journal of Geophysical Research: Solid Earth* (1993)
9. de la Iglesia Castro, D.: 3D mnist: A 3D version of the mnist database of handwritten digits. <https://www.kaggle.com/datasets/daavoo/3d-mnist>
10. Jin, K.H., McCann, M.T., Froustey, E., Unser, M.: Deep convolutional neural network for inverse problems in imaging. *IEEE Transactions on Image Processing* (2017)
11. Liu, Z., Roy, M., Prasad, D.K., Agarwal, K.: Physics-guided loss functions improve deep learning performance in inverse scattering. *IEEE Transactions on Computational Imaging* (2022)

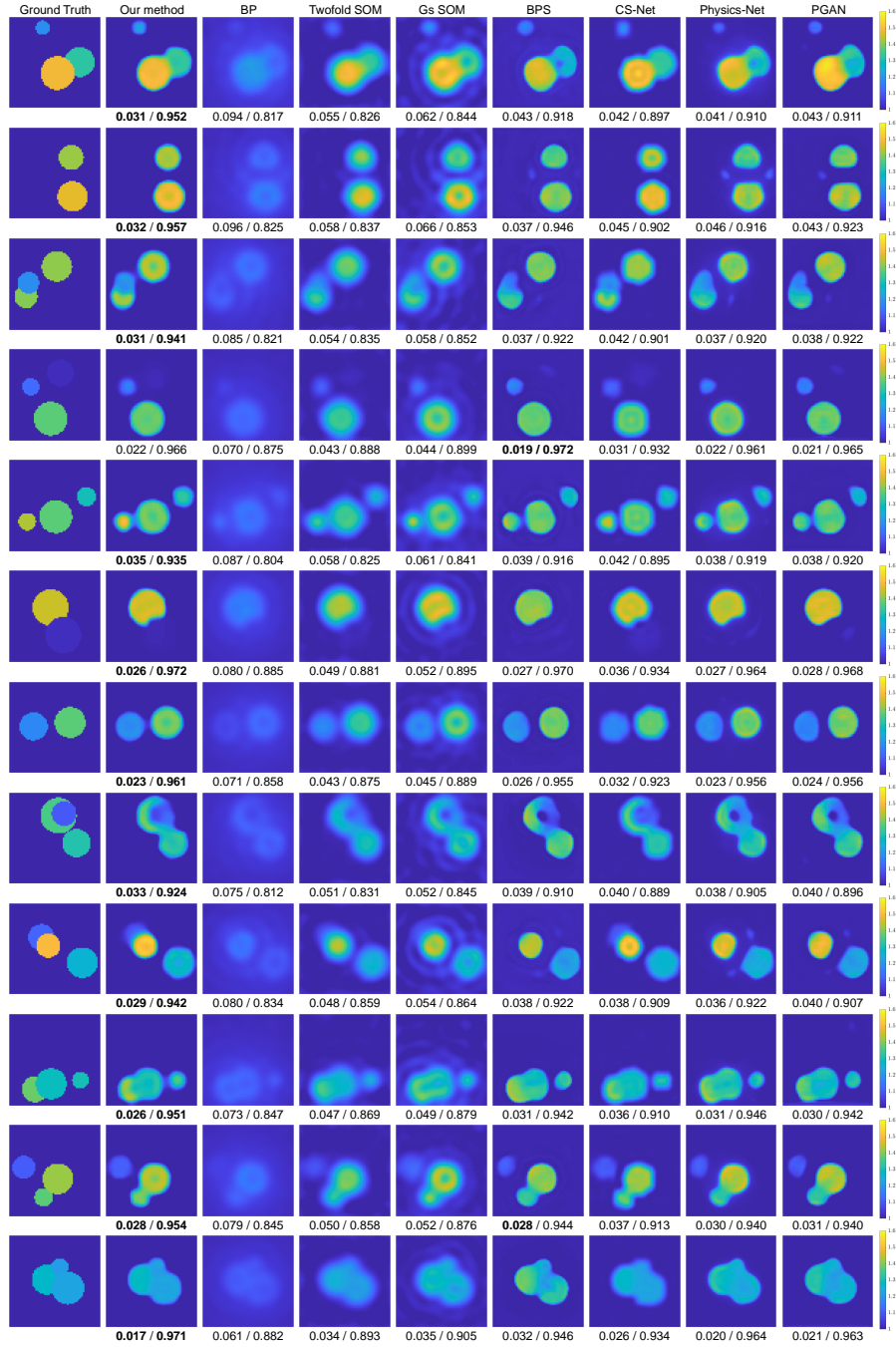


Fig. S6: Samples obtained from synthetic Circular-cylinder dataset under 5% noise level. From left to right: ground truth, results obtained by our method, BP [2], Twofold SOM [19], Gs SOM [3], BPS [18], CS-Net [14], Physics-Net [11], and PGAN [17]. RRMSE/SSIM values are shown below each figure.

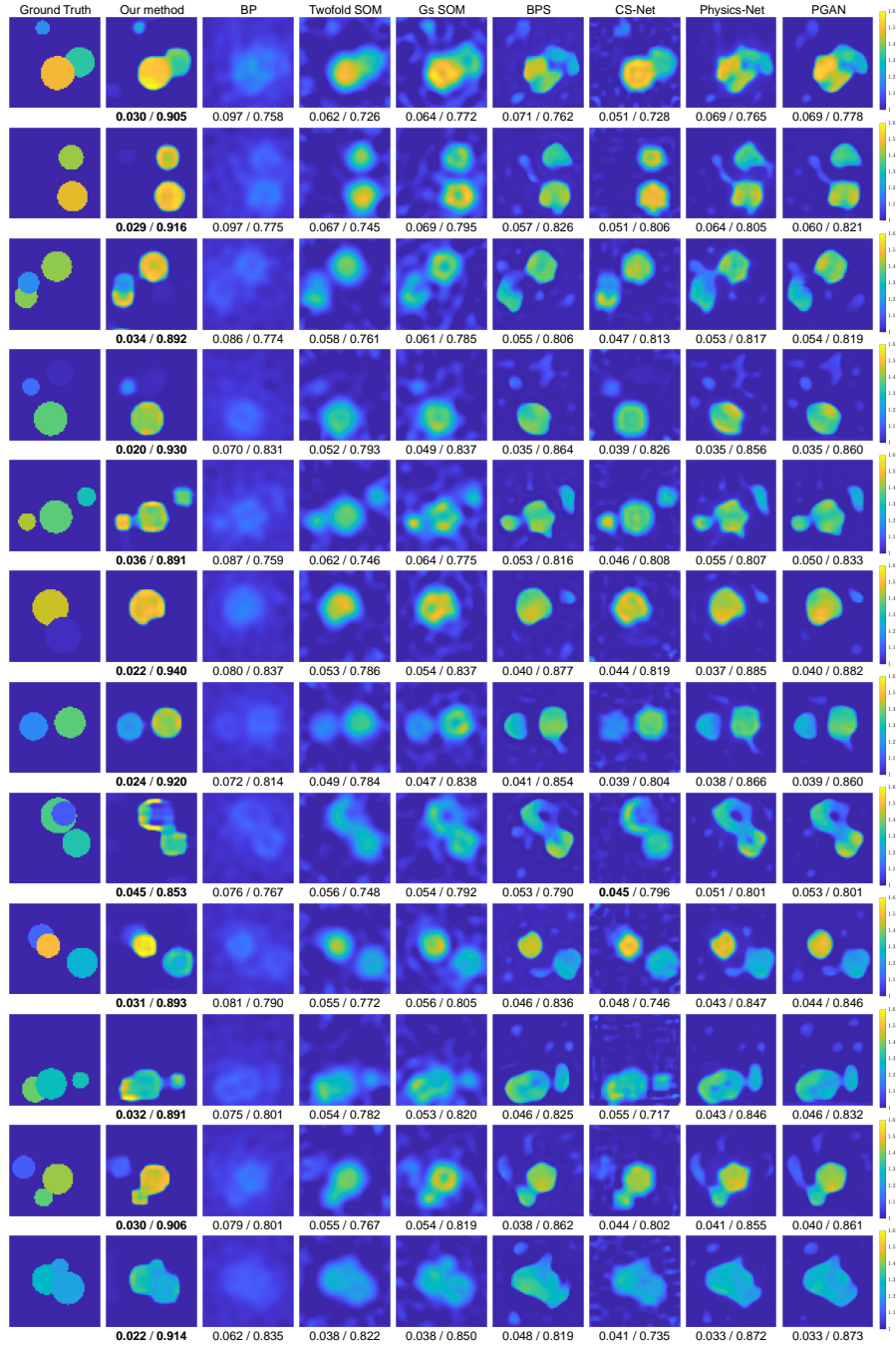


Fig. S7: Samples obtained from synthetic Circular-cylinder dataset under 30% noise level. From left to right: ground truth, results obtained by our method, BP [2], Twofold SOM [19], Gs SOM [3], BPS [18], CS-Net [14], Physics-Net [11], and PGAN [17]. RRMSE/SSIM values are shown below each figure.

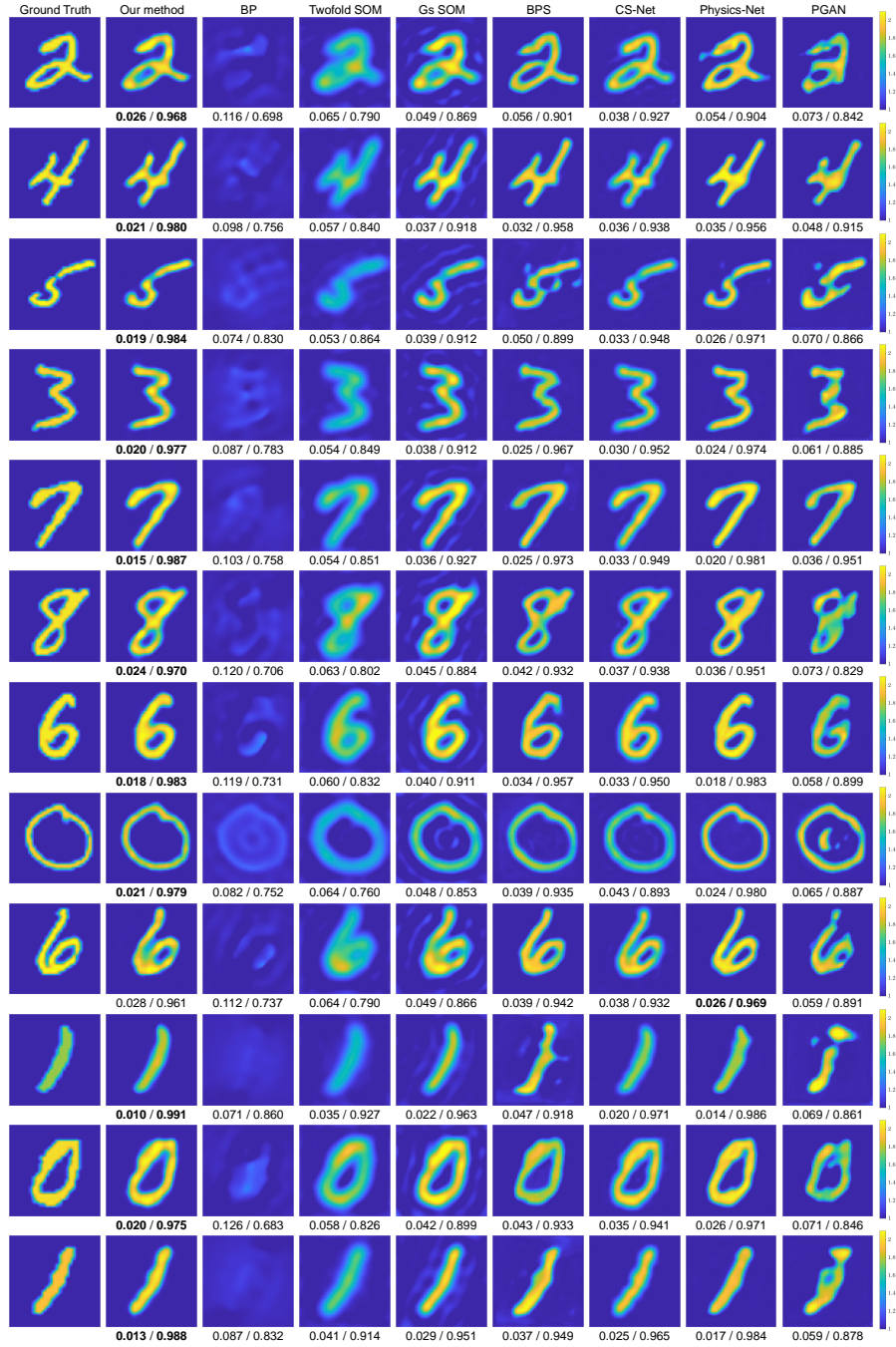


Fig. S8: Samples obtained from synthetic MNIST dataset under 5% noise level. From left to right: ground truth, results obtained by our method, BP [2], Twofold SOM [19], Gs SOM [3], BPS [18], CS-Net [14], Physics-Net [11], and PGAN [17]. RRMSE/SSIM values are shown below each figure.

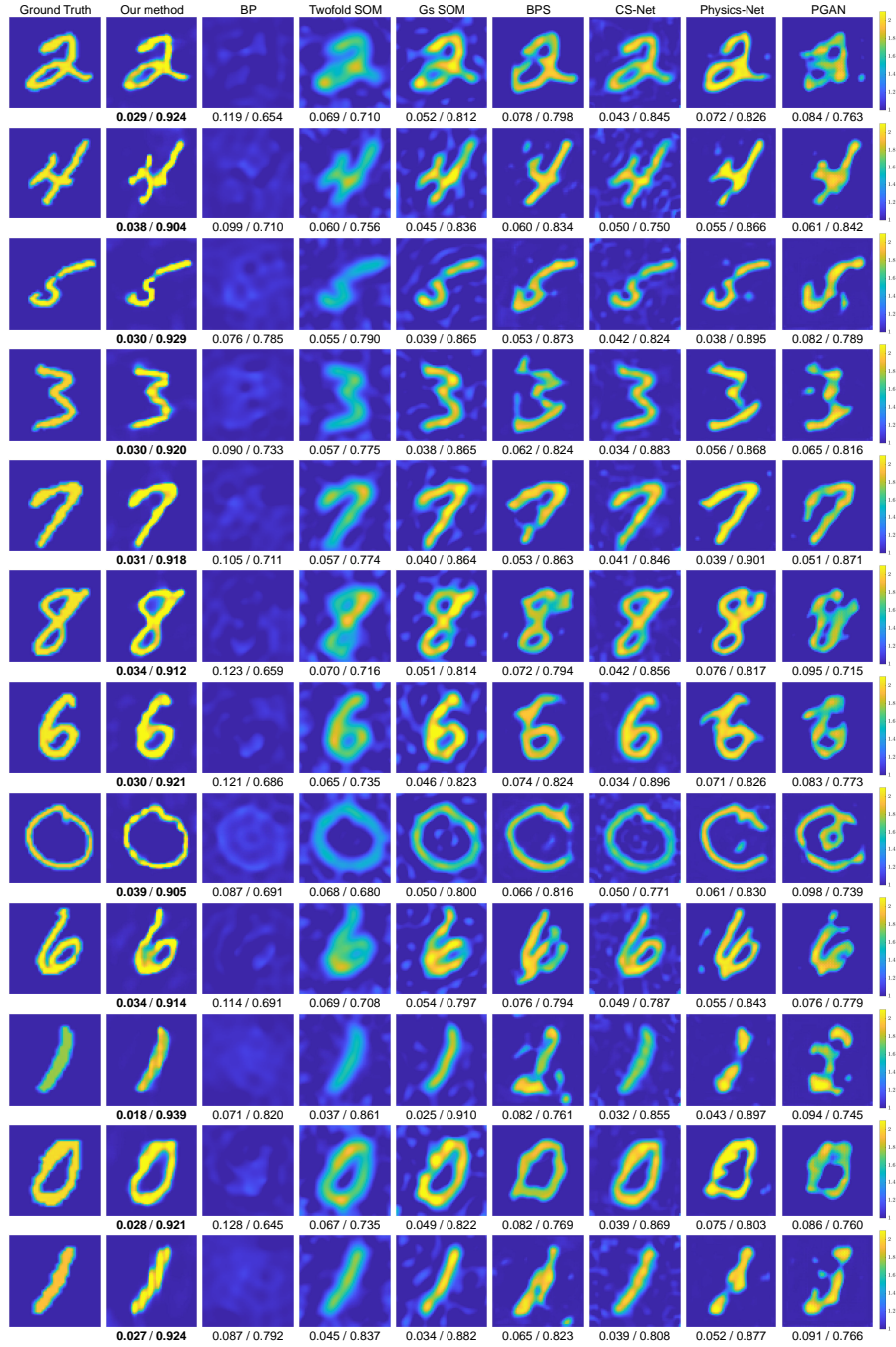


Fig. S9: Samples obtained from synthetic MNIST dataset under 30% noise level. From left to right: ground truth, results obtained by our method, BP [2], Twofold SOM [19], Gs SOM [3], BPS [18], CS-Net [14], Physics-Net [11], and PGAN [17]. RRMSE/SSIM values are shown below each figure.

12. Müller, T., Evans, A., Schied, C., Keller, A.: Instant neural graphics primitives with a multiresolution hash encoding. *ACM Transactions on Graphics (ToG)* (2022)
13. Peterson, A.F., Ray, S.L., Mittra, R.: *Computational methods for electromagnetics*. IEEE Press New York (1998)
14. Sanghvi, Y., Kalepu, Y., Khankhoje, U.K.: Embedding deep learning in inverse scattering problems. *IEEE Transactions on Computational Imaging* (2019)
15. Sitzmann, V., Martel, J., Bergman, A., Lindell, D., Wetzstein, G.: Implicit neural representations with periodic activation functions. In: *Advances in Neural Information Processing Systems* (2020)
16. Slaney, M., Kak, A., Larsen, L.: Limitations of imaging with first-order diffraction tomography. *IEEE Transactions on Microwave Theory and Techniques* (1984)
17. Song, R., Huang, Y., Xu, K., Ye, X., Li, C., Chen, X.: Electromagnetic inverse scattering with perceptual generative adversarial networks. *IEEE Transactions on Computational Imaging* (2021)
18. Wei, Z., Chen, X.: Deep-learning schemes for full-wave nonlinear inverse scattering problems. *IEEE Transactions on Geoscience and Remote Sensing* (2018)
19. Zhong, Y., Chen, X.: Twofold subspace-based optimization method for solving inverse scattering problems. *Inverse Problems* (2009)
20. Zhou, H., Cheng, Y., Zheng, H., Liu, Q., Wang, Y.: Deep unfolding contrast source inversion for strong scatterers via generative adversarial mechanism. *IEEE Transactions on Microwave Theory and Techniques* (2022)